

Novel design of Reconfigurable Tracked Robot with Geometry-Changing Tracks

Chice Xuan^{† 1,4}, Jiadong Lu^{† 1,2,3,4}, Zhihao Tian^{1,4}, Jiacheng Li^{1,4}, Mengke Zhang^{1,2,4}, Hanbin Xie^{1,4}, Jianxiong Qiu⁵, Chao Xu^{1,2,4} and Yanjun Cao^{1,2,4}

Abstract— Tracked robots with reconfigurable mechanisms exhibit great maneuverability due to their adaptability to complex ground conditions. Reconfigurable tracked robots with geometry-changing tracks show further obstacle-crossing capabilities with compact dimensions. However, existing systems face deployment limitations due to either complex transmission mechanisms or unsustainable designs when maintaining the tension in the tracks. To address these challenges, we introduce a novel design of a reconfigurable tracked robot with geometry-changing tracks, which achieves strong terrain traversability with good mechanical properties. We achieve the elliptical trajectory of key planetary wheels through a novel Quad-slider Elliptical Trammel Mechanism (Qs-ETM), allowing the tracks to maintain fixed tension while changing their geometry. Furthermore, the combination of direct drive motors significantly enhances its mechanical properties and agility. A detailed analysis of the kinematic and dynamic characteristics has been conducted and proved with a series of simulations. We built a fully functional prototype of the design and tested it in real-world experiments to validate its advantages. The result shows that our design can reduce the torque required by up to 68.3% and the shear stress of the flipper by up to 67.1%.

I. INTRODUCTION

Obstacle crossing capabilities are important for mobile robots to perform real-world tasks in unstructured environments, such as surveillance, reconnaissance in dangerous situations, and search and rescue in disaster response tasks. Robots are expected to be able to move on uneven ground, or even to climb obstacles and traverse in harsh terrains. Various kinds of robots have been developed with this motivations. Legged robots, including both quadruped and biped structures, equipped with specially designed algorithms, have demonstrated remarkable potential in negotiating obstacles [1]–[6]. However, legged robots require numerous motors for operation, and have low energy efficiency, and are too expensive at the same time. Combining wheels with legged robots have been proposed and have shown improved efficiency [7]–[11]. However, enhancements to obstacle-crossing capabilities in such systems are generally limited, making practical application difficult. Furthermore, there are robots

[†] Equal contribution.

This work was supported by National Nature Science Foundation of China under Grant No. 62103368. (Corresponding authors: Yanjun Cao, Chao Xu.)

¹ Huzhou Institute of Zhejiang University, Huzhou, 313000, China.

² State Key Laboratory of Industrial Control Technology, Institute of Cyber-Systems and Control, Zhejiang University, Hangzhou, 310027, China.

³ Shandong University, Jinan, 250100, China.

⁴ Huzhou Laboratory of Autonomous Intelligent Systems, Huzhou, 313000, China.

⁵ Zhejiang Zhongyan Industry Co. Ltd, Hangzhou, 310024, China.

E-mails:{yanjunhi, cxu}@zju.edu.cn



Fig. 1: Prototype of CubeTrack robot with different configurations, including configurations for climbing stairs, lifting chassis, and crossing gaps. Long flippers provide the robots with good obstacle-crossing capability by allowing the robot to adjust its configuration to a large extent.

that are controlled by few actuators to facilitate movements, such as wave-like robots [12]–[14]. Since the coordination of their mechanisms is primarily achieved through fixed mechanical structures, the robots' mobility is limited.

Tracked robots inherently possess great terrain adaptability thanks to the large ground contact surface, as shown in Fig. 2(a). When robots are equipped with flippers like Fig. 2(b) [15]–[17], they can climb obstacles and greatly improve the obstacle-crossing ability. However, the need for additional actuators introduces a relatively complex mechanical structure. Consequently, tracked robots with a single long arm connected from the center have been proposed, illustrated in Fig. 2(c) [18]–[22]. This structure demonstrated impressive terrain maneuverability through unstructured environments with geometry-changing tracks. The long arm provide remarkable ability to climb obstacle with single one extra degree-of-freedom involved. However, the key challenge of this proposal is how to maintain the tension within the track fixed as long as the arm rotates. Simple spring-based tension mechanism can barely provide enough range caused by the fixed length of track if the planetary wheel rotate in a elliptical trajectory. Therefore, researchers focus on how to let the planetary wheel move along the elliptical path to keep

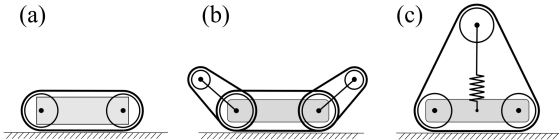


Fig. 2: Different mechanisms of tracked robots. (a) A standard tracked robot. (b) A tracked robot equipped with flippers. (c) A tracked robot with geometry-changing tracks.

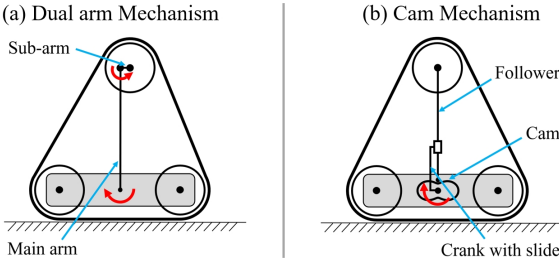


Fig. 3: Two implementations for tracked robots with geometry-changing tracks: (a) Dual-arm mechanism, and (b) Cam mechanism.

the required track length fixed, remove the tension change caused by the mechanism. Iwamoto and Yamamoto [18] proposed a dual arm structure, shown in the Fig. 3(a). The main arm and sub arm are synchronized through the combination of gears and chains to realize the elliptical trajectory. Yet, such complex synchronizing mechanism interferes with the vehicle body, limiting the range of the flipper rotation. Ben-Tzvi et al. proposed a design [19] achieving elliptical motion of the planetary wheel through a cam mechanism, which is shown in Fig. 3(b). However, as the sliding contact between the cam and the follower, which features higher pairs, the cam profile is subject to damage, especially when shocks happen while crossing obstacles. Any damage to the cam mechanism can hinder the robot's ability to transform, compromising its operational functionalities. Furthermore, both robots use a motor located in the center of chassis to drive the arm, necessitating substantial torque when lift the chassis for special tasks.

In this work, we introduce a novel design of reconfigurable tracked robot, CubeTrack, with geometry-changing tracks. We retain the advantages of the geometry changing tracks while revising the implementation to address the drawbacks. A tensioner is adopted to sustain the tension of track, achieving the elliptical motion of planetary wheel. In contrast to the previous cam mechanism, we propose a novel Quad-slider Elliptical Trammel Mechanism (Qs-ETM) within the track framework. This advancement, synergized with the integration of direct-drive (DD) motors, significantly enhances the mechanical attributes of the robot. Moreover, previous kinematic studies on reconfigurable tracked robots were specific to scenarios like stair climbing while having limited accuracy [20], [23]. We have meticulously conducted a series of accurate and empirical analysis of the kinematics. And through force analysis, we have demonstrated that our innovative design is capable of reducing the torque required for motor that drives the flipper and decreasing the shear forces experienced by the flippers. To validate the new design and prove its advancement, we built a prototype, and conducted both simulations and empirical experiments.

In particular, this paper presents the following contributions:

- 1) A novel design of a reconfigurable tracked robot with geometry-changing tracks, which achieves strong terrain traversability and good mechanical properties.
- 2) A novel Qs-ETM has been proposed for the tracked robot, allowing the tracks to maintain fixed tension while changing their geometry.
- 3) The kinematics and dynamics analysis of the design and the advantages are proved.
- 4) A fully functional prototype was built to demonstrate the feasibility, and real-world experiments are conducted to validate its advantages.

II. SYSTEM DESIGN

A. Overall Design

The main goal when designing CubeTrack is to produce a robot that is structurally compact, durable, and retains high obstacle-crossing capabilities. To achieve this, we have proposed innovative structures to realize a reconfigurable tracked robot with geometry-changing tracks. The design of CubeTrack follows modular design principle, as shown in Fig. 4. Two geometry-changing track modules (GCTM) are connected with a chassis module in middle.

Chassis module, depicted in Fig. 4(a) and Fig. 4(b), contains low-level control board, main onboard computer, and a battery inside. At the same, there are two suspension modules on both sides of the chassis, which are used to connect with the GCTM. The suspension is equipped with springs and guide shafts to filter the vibration caused by the chassis as shown in Fig. 4(b). In the future, other workloads, such as robot arms, are possible to be added to the chassis.

Geometry-changing track module is the key module features the CubeTrack. Demonstrated in Fig. 4(c), it contains the Qs-ETM and a track assembly. **Qs-ETM** enables the flipper arm to rotate along an elliptical path. The flipper has a spring translation mechanism at its end to mount the planetary sprocket, which provides limited tension adjustment control for the track. The principle and implementation of Qs-ETM is detailed in next section. **Track assembly** is composed of a planetary sprocket, two body sprockets, three DD motors, four support rollers, and a rubber track. Two body sprockets are installed at the front and rear ends of the chassis, and the planetary sprocket is mounted at the end of the flipper, acting as the planetary wheel. By incorporating the compact and lightweight DD motors into the sprockets and the planetary wheel, the robot's design is streamlined. These motors provide precise control and quick response, significantly improving the robot's agility.

By adjusting the relative velocity between the planetary wheel and the sprocket, the tension produced by the track facilitates the planetary wheel to rotate the flipper arm. The motion can be viewed as the planetary wheel actively moving in an orbit to control the flipper arm rotating, but actually with a geometry-changing orbit of soft tracks. This scheme significantly mitigates the torque demand on the motor, optimizing the force acting on the flipper.

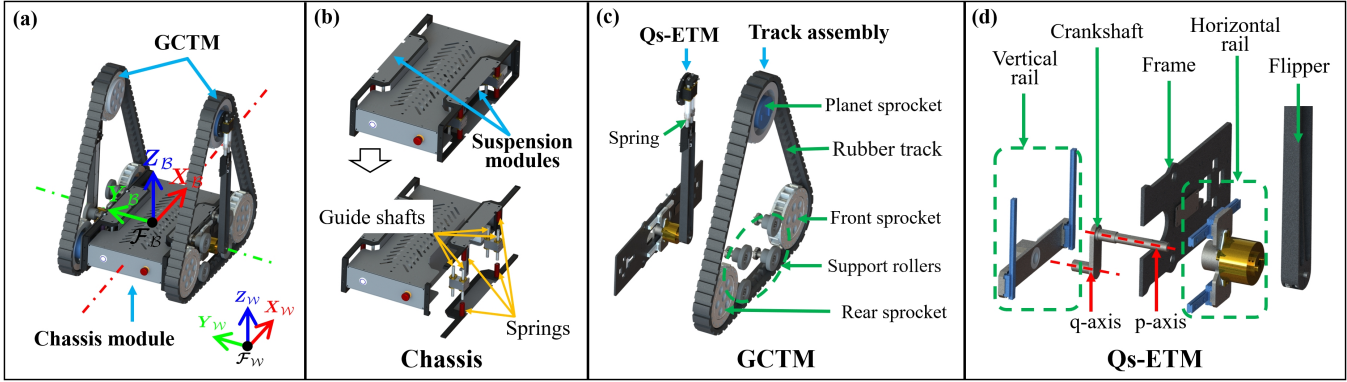


Fig. 4: The mechanism design of CubeTrack. (a) Overview of CubeTrack, (b) Chassis module design, (c) Geometry-changing track module, and (d) Quad-slider elliptical trammel mechanism.

B. Principle and implementation of Qs-ETM

Qs-ETM follows the principle of the trammel of Archimedes to generate an elliptical trajectory. However, the trammel mechanism is not easy to be practically applied in our robot. The standard trammel mechanism consists of two shuttles in the perpendicular rails and a bar attached to the shuttles by pivots. The discontinuous contact of the cross setup results in poor load-bearing capacity. Therefore we design a new Qs-ETM mechanism to solve the practical application of the trammel.

Qs-ETM consist of three parts, four set of guide rails and sliders, and a flipper as shown in Fig. 4(d). **Guide rails** consist of two sets. The horizontal and vertical rails are installed on two sides of the frame, and parallelly installed to ensure the correct sliding direction. **Sliders** are attached to cooresponding rails. Two parallel axes of the crankshaft, *p*-axis and *q*-axis, pass through the centers of the sliders by revolute joints, thus synchronizing the slider motion. **Flipper** is fixed to the *p*-axis of the crankshaft through a keyed joint, ensuring that the movement and rotation of the sliders are effectively transmitted. Compared to the previously mentioned cam mechanism, Qs-ETM contains surface contact between components, the mechanism features lower pairs, and therefore are more durable.

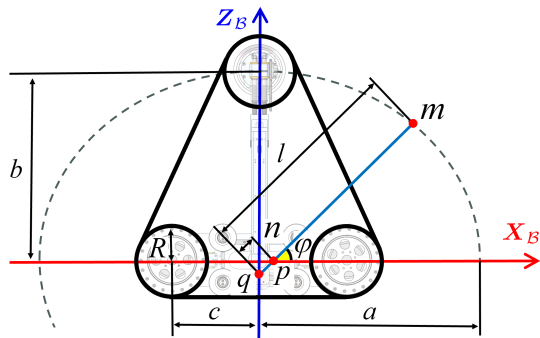


Fig. 5: Principle of Qs-ETM and the elliptical trajectory of the planetary wheel.

Fig. 5 illustrates the elliptical trajectory of the planetary wheel. Point *m* refers to the end of the flipper, also as the center of the planetary wheel, with the coordinate of (x_m, z_m) . The trajectory of the planetary wheel can be

formulated as follows:

$$\begin{cases} x_m = (l_{mp} + l_{pq}) \cos \varphi \\ z_m = (l_{mp}) \sin \varphi \end{cases} \quad (1)$$

l_{*+} is the length from point * to + shows in Fig. 5. φ is the angular displacement of flipper as listed in Table I (note that all symbols used more than once are listed in Table I). The formed dashed ellipse is characterized by its foci of sprockets, separated by a distance of $2c$, and its semi-major and semi-minor axes, denoted by a and b , respectively. Considering in conjunction with the dimensions of components, the parameter specifications yield the following relationship:

$$l = a = b + n \quad (2)$$

$$S = 2a + 2c + 2\pi R \quad (3)$$

where the length of flipper, the distance between crankshaft axes, the track length and the wheel radius are denoted by l , n , S and R , respectively. Detailed specifications of a prototype robot developed according to this design are provided in Section IV

III. KINEMATIC AND DYNAMIC ANALYSIS

In this section, we conduct detailed analyses of kinematics and dynamics. The kinematic analysis firstly presents a kinetic model considering slippage for accurate motion control in the future. Then we explore the relationships between flipper angle, planetary wheel rotation, and vehicle body angle used for body attitude control. The dynamic part examines changes in the center of mass (CoM) with the flipper angle and explores how our design improvements reduce motor torque needs and optimize flipper force.

We define the body frame $\mathcal{F}_B(X_B, Y_B, Z_B)$ with its origin at the vehicle body's geometric center and the positive X_B pointing the body's forward movement, and the inertial world frame $\mathcal{F}_W(X_W, Y_W, Z_W)$, same as in Fig. 4. The right superscript denotes the coordinate system for the variable. Unless noted, all angles are in $[-\pi, \pi]$.

A. Kinematic Modeling with Slippage Compensation

Due to slippage between the tracks and the ground, the motion of tracked vehicles cannot be accurately represented by a simple differential drive model. In this section, we utilize a kinematic model that accounts for slippage to estimate

TABLE I: Notations

Subscripts		Definitions
$C^{\mathcal{F}_B}$	{track, mech, body}	CoM position of corresponding part in \mathcal{F}_B
a, b, c	—	Ellipse parameters as shown in Fig. 5
α	—	Pitch angle of chassis
β	—	Angle between the flipper and X_W
φ	—	Angular displacement of flipper in \mathcal{F}_B
θ	—	Angular displacement of planetary wheel
w	{f, r, pw}	Identifier of the front, rear sprocket and planetary wheel
P	\forall	Positions of any objects or points
M	{B, N, P_{w_r} }	Moment of force in different positions
T	{B, N}	Torque of motors mounted at different positions
ζ	\forall	Constrain torque at any positions

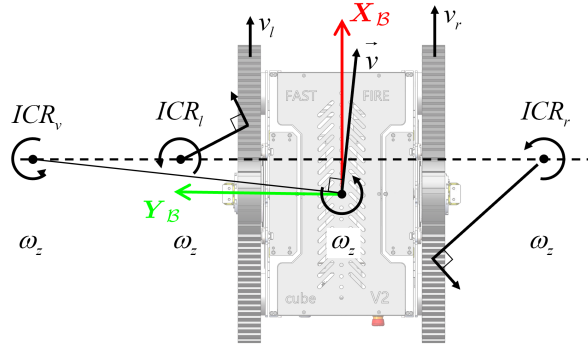


Fig. 6: The kinematics of CubeTrack.

the motion states of tracked vehicles. We adopt the method proposed by J. L. Martínez et al. [24]. They demonstrated that accurate motion estimation can be achieved through the analysis of the instantaneous centers of rotation (ICRs) of the tracks and the vehicle body.

The approximate kinematics of CubeTrack are:

$$\begin{bmatrix} v_x \\ v_y \\ w_z \end{bmatrix} = \frac{1}{y_{ICR_l} - y_{ICR_r}} \begin{bmatrix} y_{ICR_l} & -y_{ICR_r} \\ x_{ICR_l} & -x_{ICR_r} \\ -1 & 1 \end{bmatrix} \begin{bmatrix} v_r \\ v_l \end{bmatrix} \quad (4)$$

where $v = (v_x, v_y)$ represents the vehicle's translational velocity relative to \mathcal{F}_B , and w_z is its angular velocity. ICR_v denotes ICR of the entire vehicle. ICR_l and ICR_r represent the ICR of the left and right track, respectively. The exact positions of each ICR can be determined through online state estimation, as detailed in Section IV.

B. Analysis of Angles during Flipper Rotation

In previous cam design, the motor is placed at the pivot of the flipper (named Arm Driven, AD), and the planetary wheel is fully passive. The flipper rotation is same as the AD motor output and the body pitch angle is straightforward. Conversely, the introduction of the Qs-ETM and the End Wheel Driven (EWD) planetary wheel propose new relationships between the flipper angle, the planetary wheel rotation, and the body pitch angle. Through differential geometry analysis, we are able to determine the relationship between φ and θ . The starting point of the flipper is initialized along X_B . Given the transition between the tight and slack sides of the tracks, this rotation can be segmented into two discrete scenarios: $\varphi \in [0, \pi]$ and $\varphi \in [-\pi, 0]$.

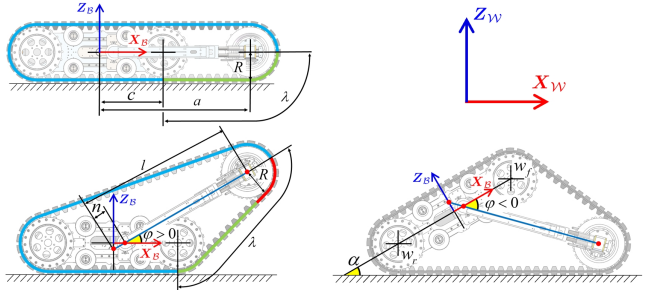


Fig. 7: Demonstration of angular displacement with varied flipper rotation angles.

As shown in Fig. 7, we define a track length, λ , as the distance from the point on the track where it intersects with the perpendicular line from front wheel w_f to the point on the track where it intersects with the extended line outward along the flipper from the planetary wheel w_{pw} .

With $\varphi \in [0, \pi]$, the relationship between φ and θ is:

$$\lambda(\varphi) = \left(\frac{\pi}{2} + \varphi \right) R + \sqrt{b^2 \cos^2 \varphi + (a \sin \varphi - c)^2} \quad (5)$$

$$\lambda(\theta) = a - c + \frac{\pi}{2} R + \theta * R \quad (6)$$

Thus, by integrating equations 5 and 6, the relationship is deduced as

$$\theta(\varphi) = \varphi + \frac{c}{R} (1 - \cos \varphi) \quad (7)$$

For the scenario within the range $[-\pi, 0]$, the analysis follows a similar process. Summarized relationship between the flipper angle and the planetary wheel angle is as

$$\theta(\varphi) = \begin{cases} \varphi + \frac{c}{R} (1 - \cos \varphi) & \varphi \in [0, \pi] \\ \varphi - \frac{c}{R} (1 - \cos \varphi) & \varphi \in [-\pi, 0] \end{cases} \quad (8)$$

Furthermore, the relationship between α and φ can be determined through geometric analysis. This relationship varies as the elevation side changes. For the scenario where the flipper lifts the body from the front, the relationship between α and φ is

$$\alpha(\varphi) = \arccos \left[\frac{c + a \cdot \cos \varphi}{a + c \cdot \cos \varphi} \right] \quad (9)$$

The relationship corresponding to the rear-lift scenario can be determined through angle conversion.

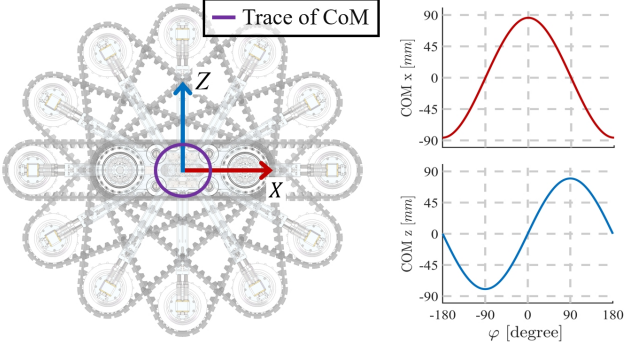


Fig. 8: Relationship between CoM position $C^{\mathcal{F}_B}$ and φ .

C. Center of Mass Analysis

The center of mass (CoM) of CubeTrack alters as the flipper rotates. Understanding the interrelation between the CoM's positional changes is crucial for analyzing the maximum angle at which the body is lifted without turning over, as well as for further analysis of dynamics.

In prior research [19], [20], the mass of the tracks was amalgamated with the total mass of the vehicle's body, rather than being assessed independently. Nevertheless, in our compactly designed robot, the mass of tracks actually takes a considerable fraction, around 17%. This signifies the impact of the tracks on the CoM in reconfigurable tracked vehicles. We formulate the position of the CoM in \mathcal{F}_B as

$$C^{\mathcal{F}_B}(\varphi) = \frac{1}{\sum m_{str}} \sum m_{str} C_{str}^{\mathcal{F}_B}(\varphi) \quad (10)$$

where m_{str} refers to the mass of corresponding components, and $str \in \{\text{body}, \text{mech}_l, \text{mech}_r, \text{track}_l, \text{track}_r\}$. $C_{\text{mech}}^{\mathcal{F}_B}$ refers to the CoM of reconfiguration mechanism, including the flipper and wheels, while $C_{\text{track}}^{\mathcal{F}_B}$ can be obtained through curve integration, as shown in Eq. 11.

$$\begin{cases} C_{\text{track}}^{\mathcal{F}_B} = \frac{b^2 \cos \varphi + s_f(c + a \cos \varphi) + s_r(c - a \cos \varphi)}{2(a + c + \pi R)} \\ C_{\text{track}}^{\mathcal{Z}_B} = \frac{b(a + s_f + s_r) \sin \varphi}{2(a + c + \pi R)} \end{cases} \quad (11)$$

where $s_f = R \cos^{-1} \frac{c+a \cos \varphi}{a+c \cos \varphi}$ and $s_r = R \cos^{-1} \frac{c-a \cos \varphi}{a-c \cos \varphi}$.

The trace of the CoM's position is illustrated in Fig. 8, where a range of 20 centimeters in each direction.

D. Motor Torque Analysis

During obstacle crossing tasks, it is common for the robot to lift itself using the flippers, where asking for substantial torque to drive the flippers. In this section, we analysis the torque requirement for both our EWD and the AD design, proving that EWD has better potential to cross obstacles.

Considering the configuration $\alpha \in [0, 90^\circ]$ shown in Fig. 9, where the sprocket w_r makes contact with the ground to elevate the vehicle body. G with subscripts refers to the gravitational force on the corresponding component. F_p denote the tension exerted by track on the planetary wheel, and F_N represents the normal force on w_{pw} .

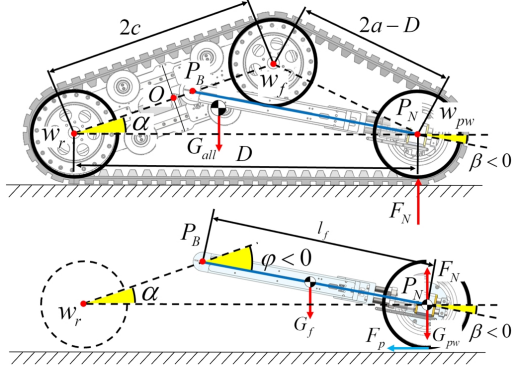


Fig. 9: Motor torque analysis between different motor install positions.

In EWD, the motor is positioned at the end of flipper, P_N . The corresponding resultant moment of the whole vehicle with respect to point w_r , along with the resultant moment of the flipper and planetary wheel with respect to P_B , and the resultant moment of the planetary wheel with respect to P_N could be expressed as:

$$\begin{cases} \sum M_{w_r} = F_N D - G_{all} |C_{all}^{X_w} - P_{w_r}^{X_w}| \\ \sum M_{P_B} = F_N l_f \cos \beta - \frac{1}{2} G_{fl} l_f \cos \beta - F_p(R - l_f \sin \beta) - G_{pw} l_f \cos \beta \\ \sum M_{P_N} = T_N - F_p R \end{cases} \quad (12)$$

In AD, the motor is positioned at the pivot of flipper, P_B . The resultant moment of the whole vehicle with respect to point w_r , and the resultant moment of the flipper and planetary wheel with respect to P_B are expressed as:

$$\begin{cases} \sum M_{w_r} = F_N D - G_{all} |C_{all}^{X_w} - P_{w_r}^{X_w}| \\ \sum M_{P_B} = F_N l_f \cos \beta - \frac{1}{2} G_{fl} l_f \cos \beta - G_{pw} l_f \cos \beta - T_B \end{cases} \quad (13)$$

Where $C_{all}^{X_w}$ represents the position of CoM along X_w , which can be determined through matrix transform.

Since the torques are balanced during stasis, by simplifying Eq. 12 and 13, we can derive the required torque for two motor positions as follows:

$$\begin{cases} T_N = \frac{F_N l_f \cos \beta - \frac{1}{2} G_{fl} l_f \cos \beta - G_{pw} l_f \cos \beta}{R - l_f \sin \beta} \cdot R \\ T_B = F_N l_f \cos \beta - \frac{1}{2} G_{fl} l_f \cos \beta - G_{pw} l_f \cos \beta \end{cases} \quad (14)$$

From Eq.14, it follows that

$$\frac{T_N}{T_B} = \frac{R}{R - l_f \sin \beta} \quad (15)$$

As the angle β is always negative ($\beta \in [-25^\circ, 0]$) when lifting itself, T_B is larger than T_N all the time. We can see the EWD design can reduce the torque required to lift itself at all angles. A similar analysis can be applied to scenarios where the wheel w_f makes contact with the ground to elevate the vehicle body.

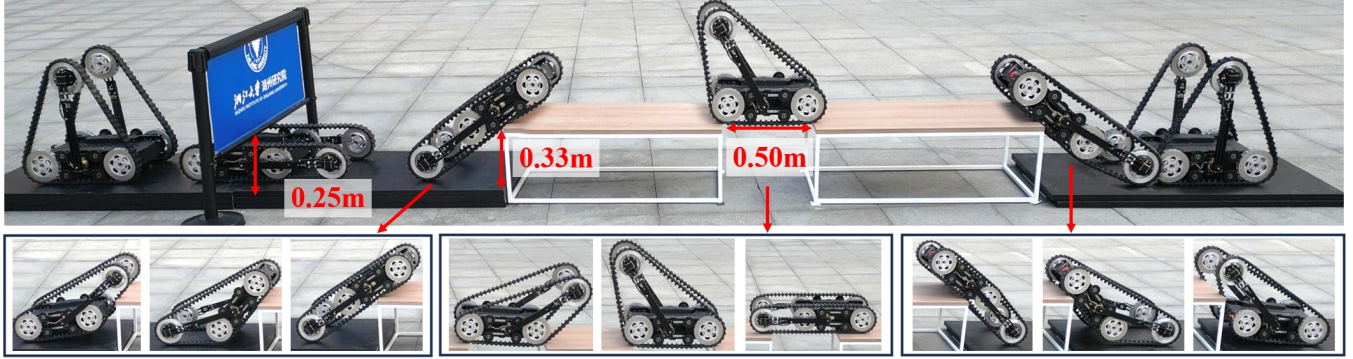


Fig. 10: Field test of CubeTrack obstacle-crossing capabilities. The robot can successfully pass low barriers close to its wheel diameter, climb obstacles much higher than its minimum height, cross gaps close to its chassis length, and smoothly move down from the obstacles.

E. Flipper Constraint Torque Analysis

In every static state, every point on the flipper is in torque equilibrium due to the presence of a constraint torque that balances the torque of the external force. The constraint torque is positively related to the shear stress experienced by the object. Hence, by analyzing the magnitude of the constraint torque, we can indirectly assess the susceptibility of the flipper to breaking.

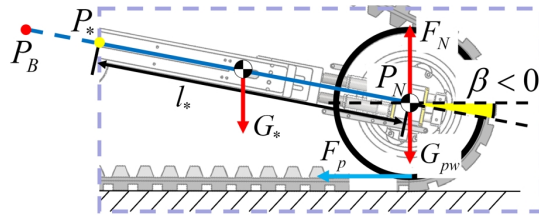


Fig. 11: Constraint torque analysis with a partial flipper for clarity.

In the same scenario as in Section III-D, we consider a segment of the flipper as shown in Fig. 11, with the length of this segment denoted as l_* . The constraint torque at the end of this segment are

$$\left\{ \begin{array}{l} {}^B\zeta_{P_*} = {}^B\mathbf{M}_{P_*} = |F_N l_* \cos \beta - G_{pw} l_* \cos \beta \\ \quad - \frac{1}{2} G_* l_* \cos \beta| \\ {}^N\zeta_{P_*} = {}^N\mathbf{M}_{P_*} = |F_N l_* \cos \beta - G_{pw} l_* \cos \beta \\ \quad - \frac{1}{2} G_* l_* \cos \beta - F_p (R - l_* \sin \beta)| \end{array} \right. \quad (16)$$

where the left superscript N, B indicate the positioning of motors, P_N or P_B , respectively. From Eq. 16, it follows that

$$|{}^B\zeta_{P_*}| - |{}^N\zeta_{P_*}| = |F_p (R - l_* \sin \beta)| \quad (17)$$

Same as Section IV-D, the angle β is always negative and ${}^B\zeta_{P_*}$ is larger than ${}^N\zeta_{P_*}$ all the time. The result proves that EWD can reduce constraint torque at every point on the flipper and outperform the AD design. A similar analysis can be applied to scenarios where the wheel w_f makes contact with the ground.

IV. EXPERIMENT

To verify the accuracy of the kinematic model and ascertain the benefits of our design, we built a prototype based on the proposed design. The specifications and obstacle-crossing performance metrics are listed in Table II and Table III. We conducted a series of simulations and real-world tests. The experiments were performed using the prototype or simulation model with identical specifications listed in Table II. RecurDyn was used in the dynamic simulations and finite element analysis.

TABLE II: CubeTrack Specifications

Specification	Dimensions		
Flipper Length	Triangle	Length	650 mm
Crankshaft Axes Distance		Width	528 mm
Wheel Radius	Flat	Height	700 mm
Track Perimeter		Length	960 mm
Mass	Flat	Width	528 mm
Max. Speed		Height	215 mm

A. Experiment on obstacle-crossing capability

We firstly evaluated the CubeTrack's capability in overcoming a series of obstacles as shown in Fig. 10. The process encompasses the traversal of low barriers, the climbing up and the descending from the raised platform, and the crossing of substantial gaps. These tests were completed with remote manipulation by an operator. As illustrated in Fig. 10, CubeTrack can successfully overcome all tasks. Furthermore, we tested the maximum performance metrics enumerated in Table III.

TABLE III: Performance Metrics

	Ours	Packbot [15]
Min. Clearance Height	0.22m	—
Max. Obstacle Height	0.33m	0.25m
Max. Ditch Width	0.60m	0.40m

B. Kinematic Model Verification

In this experiment, we employ the Extended Kalman Filter (EKF) [25] to estimate the $ICR_{v,l,r}$, and apply them in our kinematic model described in Eq. 5 to evaluate robot motion trajectory. We manually controlled the robot following an

“IROS” shape trajectory. During the experiment, the flipper swung repeatedly within the range of $[0, \pi]$, while the robot was controlled at an average linear velocity of $0.5m/s$ and an average angular velocity of $0.3rad/s$.

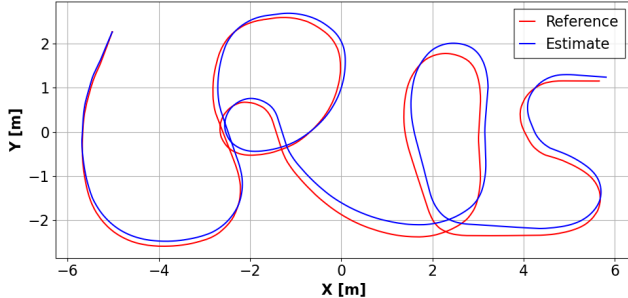


Fig. 12: Kinematics verification of CubeTrack. Comparison between the estimate path (in blue) from the kinematic model and groundtruth (in red) from motion capture system.

As shown in Fig. 12, the estimated motion trajectories in blue closely matched the ground truth trajectory from the motion capture system. Over a $44.37m$ trajectory, the maximum deviation observed was $0.37m$, attributable to shifts in the ICR precipitated by alterations in angular acceleration. Despite that EKF necessitates a temporal duration to refine the parameters, results indicate the EKF’s capability in estimating the ICR simultaneously.

C. Experiment on Motor Torque

In accordance with Eq. 14 delineated in Section III-D, we have calculated the theoretical torque necessary to elevate the vehicle for two motor placements, EWD and AD. Data of our EWD design from both the RecurDyn simulation and sensors on the prototype are collected. For the AD design, as we do not have the real robot, data only from simulation is provided.



Fig. 13: Torque analysis of CubeTrack when lifting the chassis and the simulation models of two AD and EWD designs.

In RecurDyn, we have modeled EWD and AD designs as shown in Fig. 13(b) and (c), which are abstracted and simplified for analytical purposes. Specifically, we have neglected the influence of the Qs-ETM on motor torque and replaced the motion constraints imposed by the tracks on the motors with a frictional force approximation. Further accounting for the influence of the tracks’ mass on CoM, we uniformly distribute the mass of the tracks among six motors to achieve realistic approximation. The principal distinction between the two simulation models is identified in the positioning of the drive motor for the flipper mechanism.

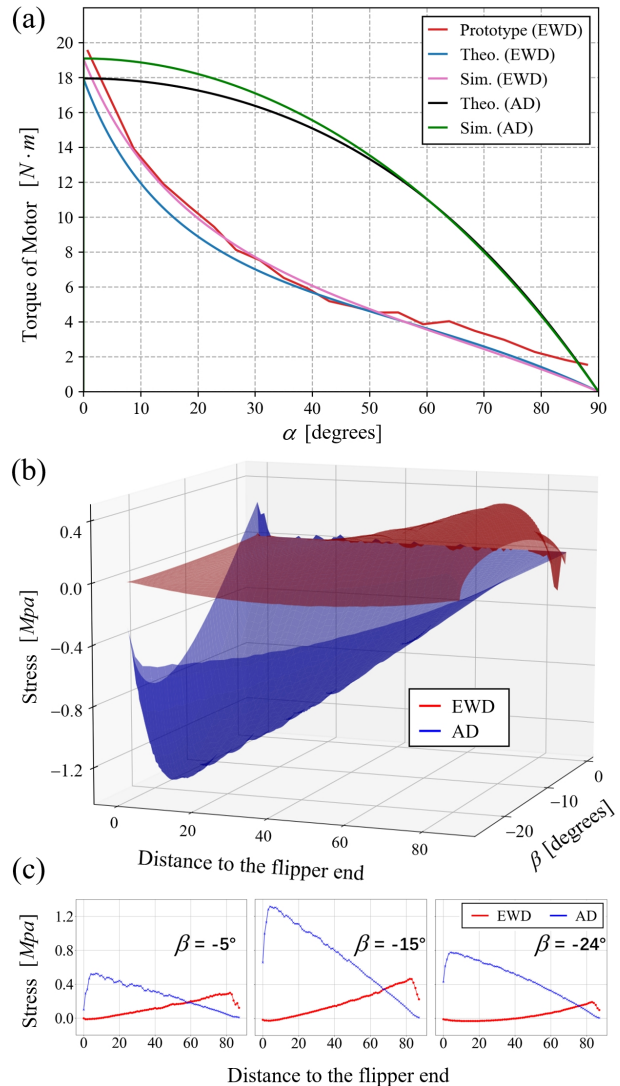


Fig. 14: (a) compares the torque required to lift the chassis among prototype tests, simulations, and theoretical analyses, with EWD and AD designs. (b) illustrates a three-dimensional graph showing how shear stress varies with the flipper angle β , collected from a set of points uniformly selected along the axis of flipper. (c) compares the shear stress along the axis of the flipper between the EWD and AD designs with three specific configurations, where the flipper angle β is at -5° , -15° and -24° .

For the prototype experiments, we controlled the angle of the flipper to decrease by 5° every 3 seconds from 0° to elevate itself. The torque is recorded from sensor after stabilization. In the simulation experiments, we recorded the motor’s torque values in all angles.

The results are depicted in Fig. 14(a). Figure shows that at the initial horizontal position, both designs require the same torque. While at any other angle, our design needs significantly less torque, decreasing by over 50% for α beyond 20° and reaching a maximum of 68.3% when $\alpha = 77.4^\circ$. These results prove the efficacy of our design in minimizing the operational torque demands, thereby enhancing the vehicle’s capability. This improvement is pivotal for overcoming obstacles, ascending and descending stairs, and elevating the body.

D. Experiment on Shear Stress of the Flipper

In this experiment, we undertook a comprehensive investigation into the stress on flippers, corresponding to the constraint torque as discussed in Section III-D. Following the models in last section, we use the finite element analysis function of RecurDyn to evaluate the shear stress of the flipper. The analysis was conducted across a range of $\alpha \in [0, \pi/2]$, between EWD and AD designs. The results show that during lifting, CubeTrack experiences significantly lower shear stress than the existing design. At the stress concentration points, the maximum shear stress of EWD is consistently over 50% lower than that of AD, reaching up to 67.1% at its peak. The simulation results show different stress concentration areas between the two designs. Stress mainly gathers around the planetary wheel in the EWD design, while the stress gathers on the pivot side for the AD design. This also makes a difference in force direction, resulting in shear stress mostly positive in our design and negative in the previous one. Results are shown in Fig. 14 b and c. For clarity, we present the magnitude of shear stress without incorporating the direction.

V. CONCLUSION

In this work, we introduce a novel design of reconfigurable tracked robot with geometry-changing tracks. We achieve the elliptical trajectory of key planetary wheels through a novel Quad-slider Elliptical Trammel Mechanism (Qs-ETM), allowing the tracks to maintain fixed tension while changing their geometry. Furthermore, the combination of direct drive motors significantly enhances its mechanical properties and agility. We built a fully functional prototype of the design and tested it in real-world experiments to validate its better performance than other designs. Looking forward, we plan to develop advanced motion planning algorithms to further enhance the robot's autonomous navigation capabilities.

REFERENCES

- [1] T. Miki, J. Lee, J. Hwangbo, L. Wellhausen, V. Koltun, and M. Hutter, “Learning robust perceptive locomotion for quadrupedal robots in the wild,” *Science Robotics*, vol. 7, no. 62, p. eabk2822, 2022.
- [2] Z. Zhuang, Z. Fu, J. Wang, C. G. Atkeson, S. Schwertfeger, C. Finn, and H. Zhao, “Robot parkour learning,” in *Conference on Robot Learning*. PMLR, 2023, pp. 73–92.
- [3] A. Kumar, Z. Fu, D. Pathak, and J. Malik, “Rma: Rapid motor adaptation for legged robots,” *Robotics: Science and Systems XVII*, 2021.
- [4] N. Rudin, D. Hoeller, P. Reist, and M. Hutter, “Learning to walk in minutes using massively parallel deep reinforcement learning,” in *Conference on Robot Learning*. PMLR, 2022, pp. 91–100.
- [5] J. Lee, J. Hwangbo, L. Wellhausen, V. Koltun, and M. Hutter, “Learning quadrupedal locomotion over challenging terrain,” *Science robotics*, vol. 5, no. 47, p. eabc5986, 2020.
- [6] J. Siekmann, Y. Godse, A. Fern, and J. Hurst, “Sim-to-real learning of all common bipedal gaits via periodic reward composition,” in *2021 IEEE International Conference on Robotics and Automation (ICRA)*. IEEE, 2021, pp. 7309–7315.
- [7] Y.-S. Kim, G.-P. Jung, H. Kim, K.-J. Cho, and C.-N. Chu, “Wheel transformer: A wheel-leg hybrid robot with passive transformable wheels,” *IEEE Transactions on Robotics*, vol. 30, no. 6, pp. 1487–1498, 2014.
- [8] S.-C. Chen, K.-J. Huang, W.-H. Chen, S.-Y. Shen, C.-H. Li, and P.-C. Lin, “Quattroped: a leg–wheel transformable robot,” *IEEE/ASME Transactions On Mechatronics*, vol. 19, no. 2, pp. 730–742, 2013.
- [9] Y. Sun and S. Ma, “Decoupled kinematic control of terrestrial locomotion for an epaddle-based reconfigurable amphibious robot,” in *2011 IEEE International Conference on Robotics and Automation*. IEEE, 2011, pp. 1223–1228.
- [10] K. Suzuki, A. Nakano, G. Endo, and S. Hirose, “Development of multi-wheeled snake-like rescue robots with active elastic trunk,” in *2012 IEEE/RSJ International Conference on Intelligent Robots and Systems*. IEEE, 2012, pp. 4602–4607.
- [11] K. Tadakuma, R. Tadakuma, A. Maruyama, E. Rohmer, K. Nagatani, K. Yoshida, A. Ming, M. Shimojo, M. Higashimori, and M. Kaneko, “Mechanical design of the wheel-leg hybrid mobile robot to realize a large wheel diameter,” in *2010 IEEE/RSJ international conference on intelligent robots and systems*. IEEE, 2010, pp. 3358–3365.
- [12] D. Shachaf, O. Inbar, and D. Zarrouk, “Rsaw, a highly reconfigurable wave robot: Analysis, design, and experiments,” *IEEE Robotics and Automation Letters*, vol. 4, no. 4, pp. 4475–4482, 2019.
- [13] T. Kislassi and D. Zarrouk, “A minimally actuated reconfigurable continuous track robot,” *IEEE Robotics and Automation Letters*, vol. 5, no. 2, pp. 652–659, 2019.
- [14] Y. Ozawa, M. Watanabe, K. Tadakuma, and S. Tadokoro, “Anisotropic-stiffness belt in mono wheeled flexible track for rough terrain locomotion,” in *2022 IEEE/RSJ International Conference on Intelligent Robots and Systems (IROS)*. IEEE, 2022, pp. 13227–13232.
- [15] B. M. Yamauchi, “Packbot: a versatile platform for military robotics,” in *Unmanned ground vehicle technology VI*, vol. 5422. SPIE, 2004, pp. 228–237.
- [16] K. Nagatani, S. Kiribayashi, Y. Okada, S. Tadokoro, T. Nishimura, T. Yoshida, E. Koyanagi, and Y. Hada, “Redesign of rescue mobile robot quince,” in *2011 IEEE international symposium on safety, security, and rescue robotics*. IEEE, 2011, pp. 13–18.
- [17] F. Michaud, D. Letourneau, M. Arsenault, Y. Bergeron, R. Cadirin, F. Gagnon, M.-A. Legault, M. Millette, J.-F. Paré, M.-C. Tremblay *et al.*, “Multi-modal locomotion robotic platform using leg-track-wheel articulations,” *Autonomous Robots*, vol. 18, pp. 137–156, 2005.
- [18] T. Iwamoto and H. Yamamoto, “Mechanical Design of Variable Configuration Tracked Vehicle.” *Journal of Mechanical Design*, vol. 112, no. 3, pp. 289–294, 09 1990. [Online]. Available: <https://doi.org/10.1115/1.2912606>
- [19] P. Ben-Tzvi, S. Ito, and A. A. Goldenberg, “A mobile robot with autonomous climbing and descending of stairs,” *Robotica*, vol. 27, no. 2, pp. 171–188, 2009.
- [20] J. Lin and A. A. Goldenberg, “Conceptual design of a variable configuration articulated tracked vehicle,” in *ASME International Mechanical Engineering Congress and Exposition*, vol. 43772, 2009, pp. 229–232.
- [21] P. Ben-Tzvi, S. Ito, and A. A. Goldenberg, “Autonomous stair climbing with reconfigurable tracked mobile robot,” in *2007 International Workshop on Robotic and Sensors Environments*. IEEE, 2007, pp. 1–6.
- [22] Y. Liu and G. Liu, “Track-stair and vehicle-manipulator interaction analysis for tracked mobile manipulators climbing stairs,” in *2008 IEEE International Conference on Automation Science and Engineering*. IEEE, 2008, pp. 157–162.
- [23] P. Ben-Tzvi, S. Ito, and A. A. Goldenberg, “A mobile robot with autonomous climbing and descending of stairs,” *Robotica*, vol. 27, no. 2, pp. 171–188, 2009.
- [24] J. L. Martínez, A. Mandow, J. Morales, S. Pedraza, and A. García-Cerezo, “Approximating kinematics for tracked mobile robots,” *The International Journal of Robotics Research*, vol. 24, no. 10, pp. 867–878, 2005.
- [25] J. Pentzer, S. Brennan, and K. Reichard, “Model-based prediction of skid-steer robot kinematics using online estimation of track instantaneous centers of rotation,” *Journal of Field Robotics*, vol. 31, no. 3, pp. 455–476, 2014.